

## Significance of Navier's slip and Arrhenius energy function in MHD flow of Casson nanofluid over a Riga plate with thermal radiation and nonuniform heat source

Manik Das\* and Bidyasagar Kumbhakar†

*Department of Mathematics,  
National Institute of Technology Meghalaya,  
Shillong 793003, India  
\*manikdas@nitm.ac.in  
†bkmath@nitm.ac.in*

Ali J. Chamkha

*Faculty of Engineering,  
Kuwait College of Science and Technology,  
Doha District, 35004, Kuwait  
a.chamkha@kcst.edu.kw*

Received 28 November 2022

Revised 21 February 2023

Accepted 4 March 2023

Published 17 June 2023

Riga plate is known to create a crossing electric and magnetic field to generate a wall-parallel Lorentz force. The significance of Casson nanofluid flow past a Riga plate is observed in the sphere of engineering, such as polymer extrusion, food manufacturing, plastic films, oil reserves and geothermal manufacturing. Researchers are interested in this model because of its potential use in biological rheological models. As Casson nanofluid flows are of great interest, this study aims to investigate the three-dimensional magnetohydrodynamics (MHD) flow with heat and mass transport of Casson nanofluid over a flat Riga plate. As a novelty, this study also includes the effectiveness of wall velocity slip, activation energy, nonlinear radiation, and temperature and space-dependent heat source/sink. Suitable similarity transformations have been employed to generate the dimensionless ordinary differential equations (ODEs) from the partial differential equations (PDEs) regulating the fluid flow problem. The transformed nonlinear boundary value problem is then solved numerically using the in-built routine "bvp4c" in MATLAB. The visual demonstrations are provided for the effects of various significant physical factors on the flow, heat and mass distributions. On the other hand, wall shear stress and rates of heat and mass transport at the surface are measured and displayed numerically in tabular form. The findings indicate that the fluid velocity in both directions slows as the velocity slip parameter increases. However, the velocity profile is escalated with the boost of modified Hartmann number. An increase in heat source parameters leads to decrease the heat transmission rate at the wall. The higher values of the radiation parameter result in a better wall heat transmission rate. Further, the rate of mass transport drops when the activation energy parameter is hiked.

† Corresponding author.

**Keywords:** Riga plate; magnetohydrodynamics (MHD); activation energy; thermal radiation; chemical reaction.

**PACS numbers:** 44.40.+a, 47.10.-g, 47.10.ad, 47.45.Gx, 47.70.Fw, 52.30.Cv.

## Nomenclature

- $u, v, w$  : Velocity components ( $\text{m} \cdot \text{s}^{-1}$ )  
 $x, y, z$  : Space coordinates (m)  
 $T_\infty$  : Ambient temperature (K)  
 $C_\infty$  : Ambient concentration ( $\text{kg} \cdot \text{m}^{-3}$ )  
 $n$  : Fitted rate constant  
 $k_r^2$  : Chemical reaction coefficient  
 $u_w, v_w$  : Stretching velocities ( $\text{m} \cdot \text{s}^{-1}$ )  
 $M_0$  : Magnetization in magnets (Tesla)  
 $k$  : Thermal conductivity ( $\text{W} \cdot \text{m}^{-1} \cdot \text{K}^{-1}$ )  
 $P, Q$  : Heat generation parameters  
 $D_B$  : Mass diffusivity ( $\text{m}^2 \cdot \text{s}^{-1}$ )  
 $c_p$  : Specific heat  
 $T$  : Temperature (K)  
 $C$  : Concentration ( $\text{kg} \cdot \text{m}^{-3}$ )  
 $T_w$  : Surface temperature (K)  
 $C_w$  : Surface concentration ( $\text{kg} \cdot \text{m}^{-3}$ )  
 $j_0$  : Current density ( $\text{A} \cdot \text{m}^{-2}$ )  
 $k^*$  : Mean absorption coefficient ( $\text{m}^{-1}$ )  
 $a_1$  : Spacing between magnets and electrodes (m)  
 $N_1, N_2$  : Slip coefficients  
 $E_a$  : Dimensional activation energy  
 $D_T$  : Coefficient of thermal diffusion ( $\text{m}^2 \cdot \text{s}^{-1}$ )  
 $\nu$  : Kinematic viscosity ( $\text{m}^2 \cdot \text{s}^{-1}$ )  
 $\mu$  : Dynamic viscosity ( $\text{kg} \cdot \text{m}^{-1} \cdot \text{s}^{-1}$ )  
 $\sigma$  : Electrical conductivity ( $\text{S} \cdot \text{m}^{-1}$ )  
 $\kappa$  : Boltzmann constant ( $\text{J} \cdot \text{K}^{-1}$ )  
 $\sigma^*$  : Stefan–Boltzmann constant ( $\text{W} \cdot \text{m}^{-2} \cdot \text{K}^{-4}$ )  
 $\theta$  : Dimensionless temperature  
 $\alpha^*$  : Thermal diffusivity ( $\text{m}^2 \cdot \text{s}^{-1}$ )  
 $\phi$  : Dimensionless concentration  
 $\rho$  : Density ( $\text{kg} \cdot \text{m}^{-3}$ )  
 $\beta$  : Casson parameter  
 $\tau$  : Ratio between effective heat capacity of nanoparticles and base fluid

## 1. Introduction

The modern industrial manufacturing process often involves the use of biological fluids such as gypsum pastes, printer inks, ceramics, lubricating greases, paints, multi-grade oils, polymers, fruit juices, blood, liquid detergents, etc.,<sup>1–3</sup> which alter the flow characteristic when stress is considered during viscosity and thus deviate from the traditional Newton's law of viscosity. Many researchers have noted this phenomenon and presented many models of non-Newtonian fluids taking into account a wide variety of flow features. Casson fluid is an extremely important non-Newtonian fluid because it accurately represents the shear-thinning property. Casson fluid acts similarly to the Newtonian fluid when the shear stress is significantly larger than the emitted stress. Casson first recognized and tallied the slowing down of printing ink due to its pigment-oil composition. Casson fluid is considered suitable rheological data, which is more effective than the model of generic viscoplasticity for various fluids. A nanofluid is a fluid in which solid nanometer-sized particles, or nanoparticles, are suspended in a base fluid with a particle size between one and one hundred nanometers. Nanoparticles in the fluid are primarily composed of carbon nanotubes, metals, carbides and oxides. These nanoparticles considerably increase the primary base fluid's thermal conductivity and convective heat transfer coefficient.<sup>4</sup> Metal or glass sheet cooling, thermal radiation, and a nonuniform heat source or sink all play crucial roles in industrial applications.<sup>5</sup> Choi pioneered a revolutionary method for combining nanoparticles with the base liquid, which resulted in an average two-fold increase in the thermal conductivity of the fluid. The widespread use of nanotechnology nowadays is a major factor in the industrial revolution. Babu and Sandeep<sup>6</sup> investigated the heat and mass transfer properties of Williamson fluid flow over a stretched sheet with varying thickness while accounting for the Soret and Dufour influences. Kumar *et al.*<sup>7</sup> studied the incompressible, electrically conducting fluid's mixed convective boundary layer flow across a plate subjected to heat radiation and an induced magnetic field. References 8–12 highlight some recent work in the field of nanofluids.

Considering several real-world applications, including nuclear reactors, semiconductor wafers, foodstuffs storage, electronic chips, etc., the influence of heat source/sink is crucial.<sup>13–18</sup> Many scientists pay close attention to heat, space-dependent, and continuous heat source/sink effects on the temperature of a wide variety of non-Newtonian liquids because heat energy is dispersed with heat source/sink effects. Different authors in different geometries have published results showing the importance of temperature and spatial dependence of heat sources and sinks in heat transference research. Heat and mass transmission properties of a non-Newtonian nanofluid flowing across a stretched surface with variable viscosity and a nonuniform heat source/sink were explored by Nagasantoshi *et al.*<sup>19</sup> On the magnetohydrodynamics (MHD) Casson nanofluid flow across a semi-infinite wavy plate, Prasad *et al.*<sup>20</sup> examined the impact of a nonuniform heat source/sink and soret. The effects of a nonuniform heat source/sink and an external magnetic field were modeled using

the semi-analytical approach homotopy analysis method (HAM), which Jakati *et al.*<sup>21</sup> applied to the flow of a Maxwell nanofluid across a linearly extending sheet. With nonuniform heat generation/absorption and motile gyrotactic microorganisms present, Kotha *et al.*<sup>22</sup> demonstrated the flow and heat transfer properties of MHD nanofluid flow through a vertical plate. Thumma *et al.*<sup>23</sup> investigated the impact of nonuniform heat source/sink and nonlinear density temperature on MHD three-dimensional (3D) Maxwell nanofluid flow across an elongated sheet numerically. The effects of heat source, Newtonian heating, and Hall and ion slip on the oblique stagnation point flow of MHD Casson nanofluid over a stretched sheet were studied by Mahmud *et al.*<sup>24</sup>

To initiate a chemical reaction, a little amount of energy, known as activation energy, is required. There is a direct correlation between the interaction of activation energy and the enhancement of a chemical phenomenon. Arrhenius's research justifies the determination and examination of the activation energy process.  $E_a$  stands for the Arrhenius activation energy, measured in kJ/mol or kcal/mol. Sometimes, activation energy is useful in food manufacturing, mechanochemistry, engineering technology, oil reserves and geothermal manufacturing.<sup>25–29</sup> Bestman described the behavior of activation energy via binary reactions that took place in a particular convective flow inside a porous channel. Hayat *et al.*<sup>30</sup> discussed the role of activation energy and binary chemical reactions in the hydromagnetic flow of a third-grade nanofluid over a nonlinearly stretched surface. Dawar *et al.*<sup>31</sup> examined the characteristic of activation energy on 2D Williamson nanofluid flow across a nonlinear stretching plate. Using the spectral local linearization approach, Shahid *et al.*<sup>32</sup> provided a numerical simulation of the effect of activation energy and buoyancy on the flow of MHD nanofluid via a vertically extended porous sheet. Taking into account viscous dissipation and Joule heating, Das and Kumbhakar<sup>33</sup> studied the effects of activation energy and Hall and ion slip on the bioconvective 3D flow of Eyring–Powell nanofluid through a convectively heated stretched sheet in a homogeneous porous media.

The Riga plate, consisting of alternating electrodes and permanent magnets installed on a flat surface, provides an effective flow in an electromagnetic actuator. Riga has a span-wise replaceable structure and is regulated by electromagnetic fields to maintain a permanent magnetism. As a result of the design of Riga plate, the Lorentz force that pushes the stream over the plate decreases exponentially. The Riga plate is an invaluable tool when it comes to minimizing the detrimental effects of turbulence and avoiding boundary layer separation. Submarines may also benefit from its ability to lessen pressure drag and friction. Gailitis and Lielausis were the first to create it. Iqbal *et al.*<sup>34</sup> investigated the effects of viscous dissipation and thermal radiation on Casson fluid flow past a Riga plate. From a theoretical perspective, Loganathan<sup>35</sup> conducted an in-depth study of the boundary layer flow of Casson fluid across a porous Riga plate, which is driven by buoyancy force. Vaidya *et al.*<sup>36</sup> investigated the effects of viscous dissipation and chemical reaction on mixed convective nanofluid flow across a thin Riga plate. Obalalu *et al.*<sup>37</sup> discussed Casson nanofluid flow caused by a stretched Riga plate under the impact of melting heat

transfer, Arrhenius activation energy, internal energy change and chemical reaction. Hussain *et al.*<sup>38</sup> demonstrated how Navier's slip condition affects the convection of a Casson-nanofluid through a vertically heated Riga plate in a mixed convection scenario. Abbas and Shatanawi<sup>39</sup> examined the cumulative effects of the Casson micropolar fluid model across a vertically variable stretched Riga sheet, taking into account Brownian motion, thermophoresis, and thermal and velocity slip impacts. Some remarkable studies in Riga plate are noted in Refs. 40–43.

From the aforementioned research studies, it is seen that no work has been reported with the effect of velocity slip and activation energy on Casson nanofluid flow past a Riga plate. This research gap led us to study how effective factors affect the flow of Casson nanofluid on the Riga plate with the help of a “*bvp4c*” solver in MATLAB. So, the following are the main goals of the current investigation:

- To provide a mathematical model for Casson nanofluid flow past a Riga plate.
- To analyze the impact of velocity slip and a nonuniform heat source/sink on Casson nanofluid.
- To examine the effect of activation energy for concentration in Casson nanofluid flow.
- To visualize the effects of the relevant factors on the velocity, temperature and concentration profiles in the Casson model.

Many industrial and technical sectors, including polymer extrusion, food production, plastic films, engineering technologies, oil reserves and geothermal manufacturing, benefit more from Casson fluid models. This study becomes more beneficial and substantial when used to biomedical science, sustainable petroleum cell talents, pharmaceutical commerce, biosensors, biological polymer amalgamation, environment responsive presentations, microbial enhanced lubricant retrieval, and biotechnology.

## 2. Mathematical Formulation of the Problem

### 2.1. Description of physical geometry

We consider a 3D steady Casson nanofluid flow with heat and mass transport over a stretching Riga plate consisting of alternating electrodes and permanent magnets. The plate is positioned in the Cartesian coordinates  $(X, Y, Z)$  in such a manner that the surface of the plate coincides with the  $XY$ -plane and the  $Z$ -axis is normal to the plate. The fluid flow is confined within the region  $Z \geq 0$ . In order to induce the fluid flow, the surface of the Riga plate is stretched with velocities  $u_w = ax$  and  $v_w = by$  ( $a, b$  being positive constants) along  $X$  and  $Y$ -directions, respectively. The presence of thermal radiation (in nonlinear form), Arrhenius activation energy function (exponential form) and nonuniform heat sources/sinks (space and time-dependent) are also incorporated into the analysis. The magnetic force, according to Grinberg's hypothesis, is expressed as  $F = \frac{\pi J_0 M(x)}{8\rho} e^{-\frac{x}{a_1 z}}$ . Also, the modified magnetic field is considered as  $M(x) = M_0 x$ . Further, Navier's slip condition at the interface between

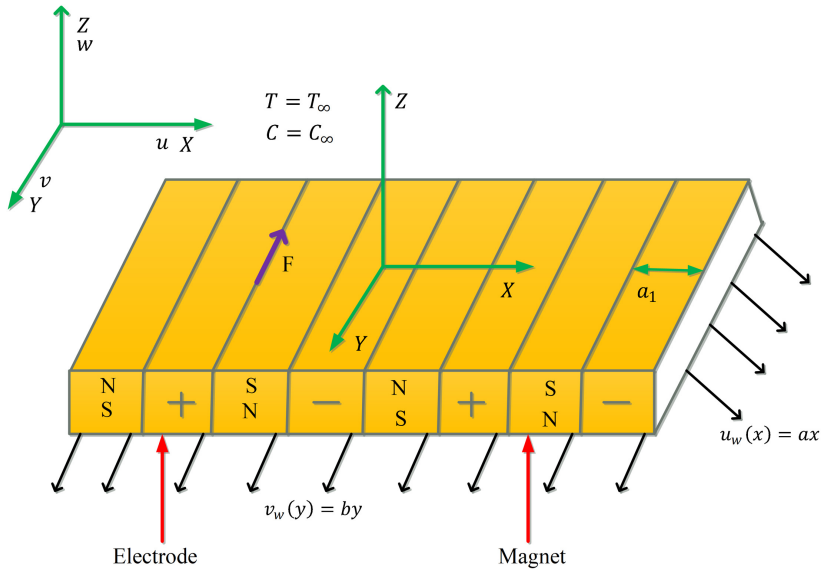


Fig. 1. (Color online) Geometry of the flow problem.

fluid and plate is imposed. An overall physical configuration of the present fluid flow problem is depicted in Fig. 1.

## 2.2. Governing equations and boundary conditions

Under the aforementioned assumptions and following Buongiorno's nanofluid model, the governing equations for velocity, temperature and concentration may be reconstructed as<sup>44,45,47</sup>

$$\frac{\partial u}{\partial x} + \frac{\partial v}{\partial y} + \frac{\partial w}{\partial z} = 0, \quad (1)$$

$$u \frac{\partial u}{\partial x} + v \frac{\partial u}{\partial y} + w \frac{\partial u}{\partial z} = \nu \left( 1 + \frac{1}{\beta} \right) \frac{\partial^2 u}{\partial z^2} + \frac{\pi J_0 M(x)}{8\rho} e^{-\frac{\pi x}{a_1}}, \quad (2)$$

$$u \frac{\partial v}{\partial x} + v \frac{\partial v}{\partial y} + w \frac{\partial v}{\partial z} = \nu \left( 1 + \frac{1}{\beta} \right) \frac{\partial^2 v}{\partial z^2}, \quad (3)$$

$$u \frac{\partial T}{\partial x} + v \frac{\partial T}{\partial y} + w \frac{\partial T}{\partial z} = \alpha \frac{\partial^2 T}{\partial z^2} + \tau \left\{ D_B \frac{\partial T}{\partial z} \frac{\partial C}{\partial z} + \frac{D_T}{T_\infty} \left( \frac{\partial T}{\partial z} \right)^2 \right\} - \frac{1}{(\rho c_p)_f} \frac{\partial q_r}{\partial z} + \frac{q''}{(\rho c_p)_f}, \quad (4)$$

$$u \frac{\partial C}{\partial x} + v \frac{\partial C}{\partial y} + w \frac{\partial C}{\partial z} = D_B \frac{\partial^2 C}{\partial z^2} + \frac{D_T}{T_\infty} \frac{\partial^2 T}{\partial z^2} - k_r^2 (C - C_\infty) \left( \frac{T}{T_\infty} \right)^n e^{-\frac{E_a}{\kappa T}}. \quad (5)$$

The following are the physical boundary conditions for the present flow problem<sup>14,45</sup>:

$$\left. \begin{aligned} u &= u_w(x) + \left(1 + \frac{1}{\beta}\right)N_1\mu \frac{\partial u}{\partial z}, & v &= v_w(x) + \left(1 + \frac{1}{\beta}\right)N_2\mu \frac{\partial v}{\partial z}, & w &= 0, \\ T &= T_w, & C &= C_w, & & \text{at } z = 0, \\ u &\rightarrow 0, & v &\rightarrow 0, & T &\rightarrow T_\infty, & C &\rightarrow C_\infty & \text{as } z \rightarrow \infty. \end{aligned} \right\} \quad (6)$$

Here, Eq. (1) is the continuity equation, whereas the principle of momentum conservation is demonstrated by Eqs. (2) and (3), known as the Navier–Stokes equations. The terms appearing on the left-hand side of Eqs. (2) and (3) are the advective terms, while the first and second term terms on the right-hand side of Eq. (2) are caused by the Casson fluid and the Riga plate, respectively. The influence of thermophoresis and Brownian motion is added by the second term on the right-hand side of the energy Eq. (4). The third and fourth components emerge as a result of the inclusion of nonlinear thermal radiation and nonuniform heat source/sink effects. Equation (5) is used to explain the concentration of nanoparticles. In this equation, the third component on the right-hand side imposes the impact of chemical reaction in addition to Arrhenius activation energy. The terms  $(1 + \frac{1}{\beta})N_1\mu \frac{\partial u}{\partial z}$  and  $(1 + \frac{1}{\beta})N_2\mu \frac{\partial v}{\partial z}$  in Eq. (6) indicate the existence of velocity slips at the surface.

The following Rosseland’s estimate for an optically thick fluid is used to approximate the radiative heat flux  $q_r$  (Ref. 46):

$$q_r = -\frac{16\sigma^*T^3}{3k^*} \frac{\partial T}{\partial z}. \quad (7)$$

The expression of space and temperature-dependent heat source/sink  $q''$  is defined as<sup>47</sup>

$$q'' = \frac{ku_w}{\nu x} \left[ \frac{P(T_w - T_\infty)}{ax} u + Q(T - T_\infty) \right]. \quad (8)$$

The energy equation has the form after applying expressions (7) and (8) to Eq. (4)

$$\begin{aligned} u \frac{\partial T}{\partial x} + v \frac{\partial T}{\partial y} + w \frac{\partial T}{\partial z} &= \alpha \frac{\partial^2 T}{\partial z^2} + \tau \left\{ D_B \frac{\partial T}{\partial z} \frac{\partial C}{\partial z} + \frac{D_T}{T_\infty} \left( \frac{\partial T}{\partial z} \right)^2 \right\} \\ &+ \frac{ku_w}{(\rho c_p)_f \nu x} \left[ \frac{P(T_w - T_\infty)}{ax} u + Q(T - T_\infty) \right] \\ &+ \frac{16\sigma^*T^2}{(3\rho c_p)_f k^*} \left\{ T \frac{\partial^2 T}{\partial Z^2} + 3 \left( \frac{\partial T}{\partial Z} \right)^2 \right\}. \end{aligned} \quad (9)$$

### 2.3. Similarity transformations

To obtain similar solutions of Eqs. (2), (3), (9) and (5) subject to the boundary conditions (6), the following similarity variables are introduced<sup>23</sup>:

$$\left. \begin{aligned} u &= axf'(\eta), \quad v = ayg'(\eta), \quad w = -\sqrt{av}(f(\eta) + g(\eta)), \quad \theta(\eta) = \frac{T - T_\infty}{T_w - T_\infty}, \\ \phi(\eta) &= \frac{C - C_\infty}{C_w - C_\infty}, \quad \eta = z\sqrt{\frac{a}{\nu}}. \end{aligned} \right\} \quad (10)$$

### 2.4. Dimensionless equations and boundary conditions

Substitution of the above similarity variables in Eqs. (2), (3), (9) and (5) yields the following ordinary differential equations:

$$\left(1 + \frac{1}{\beta}\right) f''' + (f + g)f'' - f'^2 + \text{Ha}e^{-B\eta} = 0, \quad (11)$$

$$\left(1 + \frac{1}{\beta}\right) g''' + (f + g)g'' - g'^2 = 0, \quad (12)$$

$$\begin{aligned} \theta'' + \text{Pr}(f + g)\theta' + \text{PrNb}\theta'\phi' + \text{PrNt}(\theta')^2 + (\text{Pr}f' + Q\theta) \\ + \text{Rd}\{1 + \theta(\theta_w - 1)\}^2[3(\theta')^2(\theta_w - 1) + \{1 + \theta(\theta_w - 1)\}\theta''] = 0, \end{aligned} \quad (13)$$

$$\phi'' + \text{PrLe}(f + g)\phi' + \frac{\text{Nt}}{\text{Nb}}\theta'' - \text{PrLe}K_1\{1 + (\theta_w - 1)\theta\}^n e^{-\frac{E}{1+(\theta_w - 1)\theta}}\phi = 0. \quad (14)$$

The dimensionless boundary conditions are stated as

$$\left. \begin{aligned} f'(0) &= 1 + \left(1 + \frac{1}{\beta}\right)\alpha_1 f''(0), \quad g'(0) = c + \left(1 + \frac{1}{\beta}\right)\alpha_2 g''(0), \\ f(0) &= 0, \quad g(0) = 0, \quad \theta(0) = 1, \quad \phi(0) = 1, \\ f'(\infty) &\rightarrow 0, \quad g'(\infty) \rightarrow 0, \quad \theta(\infty) \rightarrow 0, \quad \phi(\infty) \rightarrow 0, \end{aligned} \right\} \quad (15)$$

where

$$\begin{aligned} \text{Pr} &= \frac{\nu}{\alpha}, \quad \text{Ha} = \frac{\pi J_0 M_0}{8\rho a^2}, \quad \text{Nb} = \frac{\tau D_B(C_w - C_\infty)}{\nu}, \quad \text{Nt} = \frac{\tau D_T(T_w - T_\infty)}{\nu T_\infty}, \\ \alpha_1 &= N_1\mu\sqrt{\frac{a}{\nu}}, \quad \alpha_2 = N_2\mu\sqrt{\frac{a}{\nu}}, \quad K_1 = \frac{k_r^2}{a}, \quad \theta_w = \frac{T_w}{T_\infty}, \quad E = \frac{E_a}{\kappa T_\infty}, \\ \text{Rd} &= \frac{4\sigma^* T_\infty^3}{k^* K}, \quad B = \frac{\pi}{a_1}\sqrt{\frac{\nu}{a}}, \quad \text{Le} = \frac{\alpha}{D_B}, \quad c = \frac{b}{a} \end{aligned}$$

are Prandtl number, modified Hartmann number, Brownian motion parameter, thermophoresis parameter, velocity slip parameters, chemical reaction parameter, temperature ratio parameter, activation energy parameter, thermal radiation parameter, dimensionless parameter, Lewis number, and velocity ratio parameter, respectively.

### 3. Significant Physical Quantities

The significant physical quantities of interest for the present fluid flow problem are the local skin-friction coefficient ( $C_{fx}$ ), Nusselt number ( $Nu_x$ ), and Sherwood number ( $Sh_x$ ) which signify, respectively, the shear stress, rate of heat transport and rate of mass transport at the surface of the Riga plate and are defined as<sup>14</sup>

$$C_{fx} = \frac{\nu}{u_w^2} \left(1 + \frac{1}{\beta}\right) \left(\frac{\partial u}{\partial z}\right)_{z=0}, \tag{16}$$

$$C_{fy} = \frac{\nu}{v_w^2} \left(1 + \frac{1}{\beta}\right) \left(\frac{\partial v}{\partial z}\right)_{z=0}, \tag{17}$$

$$Nu_x = -\frac{x}{k(T_w - T_\infty)} \left[ \left(k + \frac{16\sigma^* T^3}{3k^*}\right) \frac{\partial T}{\partial z} \right]_{z=0}, \tag{18}$$

$$Sh_x = -\frac{x D_B}{D_B(C_w - C_\infty)} \left(\frac{\partial C}{\partial z}\right)_{z=0}. \tag{19}$$

Making use of the similarity transformations specified in Eq. (9), the aforementioned physical quantities are expressed in nondimensional form as

$$C_{fx} \sqrt{Re_x} = \left(1 + \frac{1}{\beta}\right) f''(0), \tag{20}$$

$$C_{fy} \sqrt{Re_y} = \left(1 + \frac{1}{\beta}\right) c^{-\frac{3}{2}} g''(0), \tag{21}$$

$$\frac{Nu_x}{\sqrt{Re_x}} = -[1 + Rd\{1 + (\theta_w - 1)\theta(0)\}^3] \theta'(0), \tag{22}$$

$$\frac{Sh_x}{\sqrt{Re_x}} = -\phi'(0), \tag{23}$$

where  $Re_x = \frac{u_w x}{\nu}$  and  $Re_y = \frac{v_w y}{\nu}$  are the local Reynolds numbers.

### 4. Numerical Solution Using “*bvp4c*”

The dimensionless ordinary differential equations of higher order (10)–(13) with relative boundary constraints 14 are reduced to the first-order boundary value problem. The well-known MATLAB’s *bvp4c* built-in function is used to numerically integrate the dimensionless ordinary differential equations using a shooting technique. The *bvp4c* solver is developed based on the Lobatto-IIIa formula, a finite difference scheme. One of the most consistent approaches is the *bvp4c* technique, which is superior than some of the other methods, such as the Homotopy Analysis Method, Adomian decomposition, etc. Moreover, the *bvp4c* has the tolerance of  $10^{-6}$ , which is good enough to get better accuracy in the results. Therefore, we prefer it over the other approaches to solve the current nonlinear boundary value problem.

Table 1. Comparison of  $-f''(0)$ 's numerical findings with previously published data.

	Wang <sup>48</sup>	Kumar <i>et al.</i> <sup>49</sup>	Ragupathi <i>et al.</i> <sup>50</sup>	This study
$c$	$-f''(0)$	$-f''(0)$	$-f''(0)$	$-f''(0)$
0	1	1	1	1
0.25	1.0488	1.04906	1.04881108	1.048813
0.50	1.0930	1.09324	1.09309502	1.093096
0.75	1.1344	1.13458	1.13448575	1.134485
1.00	1.1737	1.17378	1.173720	1.173720

Table 2. Comparison of  $-g''(0)$ 's numerical findings with previously published data.

	Wang <sup>48</sup>	Kumar <i>et al.</i> <sup>49</sup>	Ragupathi <i>et al.</i> <sup>50</sup>	This study
$c$	$-g''(0)$	$-g''(0)$	$-g''(0)$	$-g''(0)$
0	0	0	0	0
0.25	0.1945	0.19457	0.19456383	0.194565
0.50	0.4652	0.46532	0.46520485	0.465206
0.75	0.7946	0.79470	0.79461826	0.794618
1.00	1.1737	1.17378	1.17372074	1.173720

### 5. Comparison of Results

In this study, the numerical findings are verified by comparing those with previously reported results by Wang,<sup>48</sup> Kumar *et al.*<sup>49</sup> and Ragupathi *et al.*<sup>50</sup> for a limiting case of the ongoing problem. The comparison is depicted in Tables 1 and 2 which provide the values of  $-f''(0)$  and  $-g''(0)$  when  $Ha = \alpha_1 = \alpha_2 = 0$  and  $\beta \rightarrow \infty$ . One can easily note that our results are in close agreement with those of Wang,<sup>48</sup> Kumar *et al.*<sup>49</sup> and Ragupathi *et al.*<sup>50</sup> This justifies the correctness and accuracy of the results reported in this study.

### 6. Results and Discussion

This investigation involves a variety of relevant flow parameters, each of which exhibits specific features depending on the fluid velocity, temperature and concentration profiles. The purpose of this part is primarily to investigate the effects of these controlling factors on the flow regime. Tabular representation is also used to examine the attributes of the decreased skin friction coefficient, Nusselt and Sherwood numbers. In light of the relevant research publications, the default values for the parameters  $\beta = \alpha_1 = \alpha_2 = E = n = 0.5$ ,  $P = Q = 0.2$ ,  $Nb = Nt = 0.1$ ,  $Ha = 2$ ,  $K_1 = 1.2$ ,  $Rd = c = 0.7$ ,  $Le = 1$ ,  $Pr = \theta_w = 1.5$  and  $B = 4$  are used to generate a numerical solution.

The influence of  $Ha$  on  $f'(\eta)$  and  $g'(\eta)$  is seen in Figs. 2 and 3. Because the velocity profile rises with increasing  $Ha$  as seen in Fig. 2, the momentum boundary layer grows in thickness. Typically, the Hartmann number corresponds inversely to the

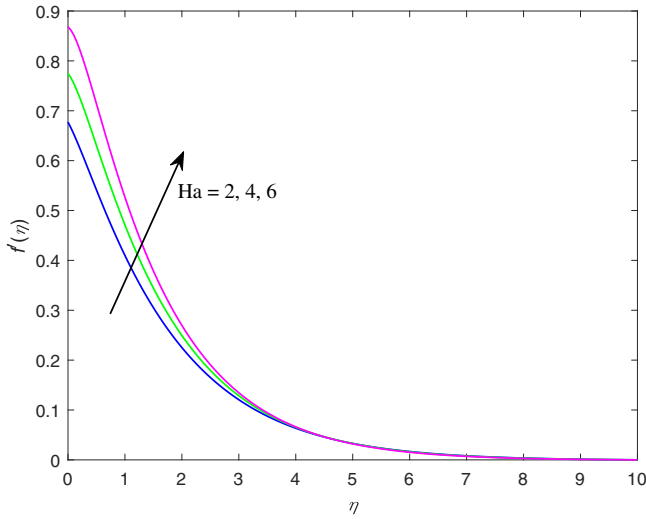


Fig. 2. (Color online)  $f'(\eta)$  under the dominance of Ha.

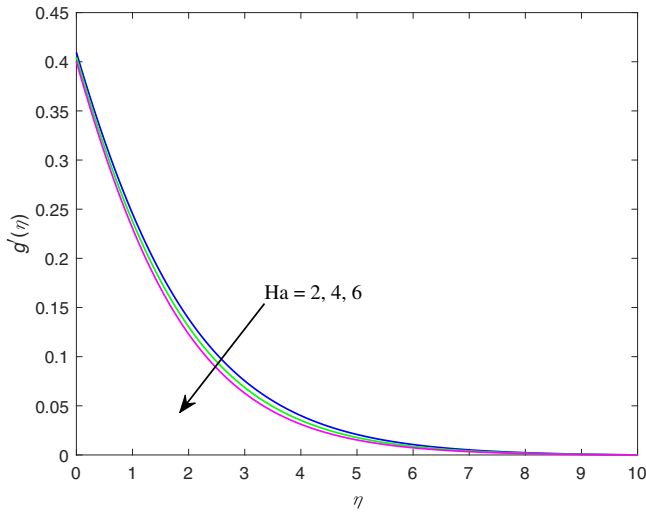


Fig. 3. (Color online)  $g'(\eta)$  under the dominance of Ha.

velocity profile. Lorentz force, generated by an array of magnets and electrodes running perpendicular to the Riga plate's surface, boosts the velocity profiles in this scenario. The typical nature is seen for  $g'(\eta)$  with growing Ha in Fig. 3. The sway of  $\beta$  on the velocity distribution is visible in Figs. 4 and 5. When  $\beta$  is amplified, the velocity field exhibits a deceleration. When the value of  $\beta$  is increased, the viscosity of the nanofluid increases, causing the yield stress and velocity profile to decrease significantly. From the velocity curves in Figs. 6 and 7, we may infer that the greater values of the slip parameters  $\alpha_1$  and  $\alpha_2$  result in a slower fluid motion. An increase in

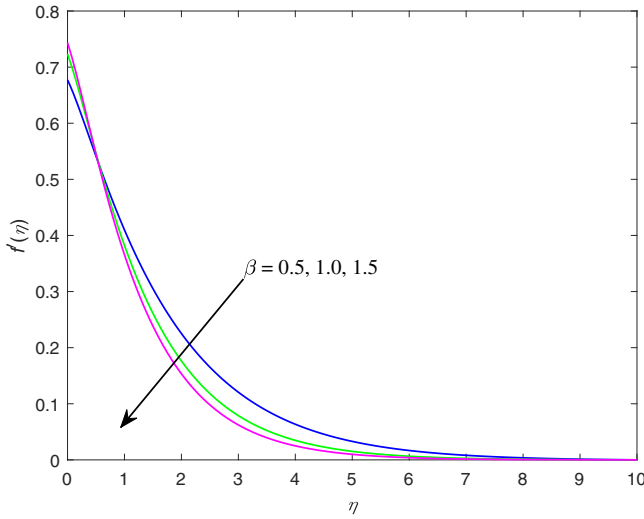


Fig. 4. (Color online)  $f'(\eta)$  under the dominance of  $\beta$ .

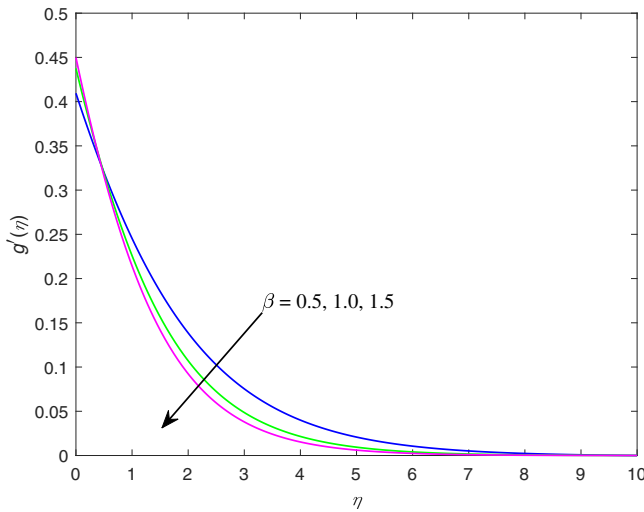


Fig. 5. (Color online)  $g'(\eta)$  under the dominance of  $\beta$ .

the velocity slip parameters implies more slippage between the plate's surface and the fluid. So, only a part of the stretching velocity is passed on to the fluid, which slows it down. Figure 8 illustrates that when  $Ha$  increases, the fluid temperature drops. A higher Lorentz force is created when the magnetic parameter rises. This force is responsible for the cooling of a fluid. Figure 9 depicts the influence of  $Rd$  on thermal profile. Raising  $Rd$  values results in an improvement to the thermal profile. This is because when  $Rd$  grows, the mean absorption coefficient decreases and this decrease

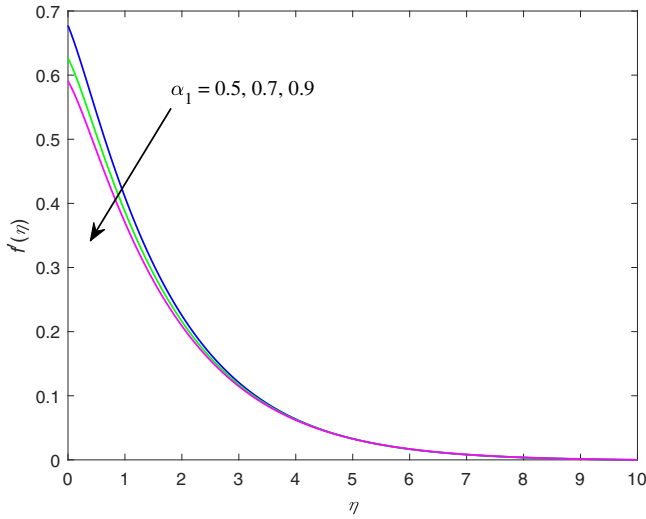


Fig. 6. (Color online)  $f'(\eta)$  under the dominance of  $\alpha_1$ .

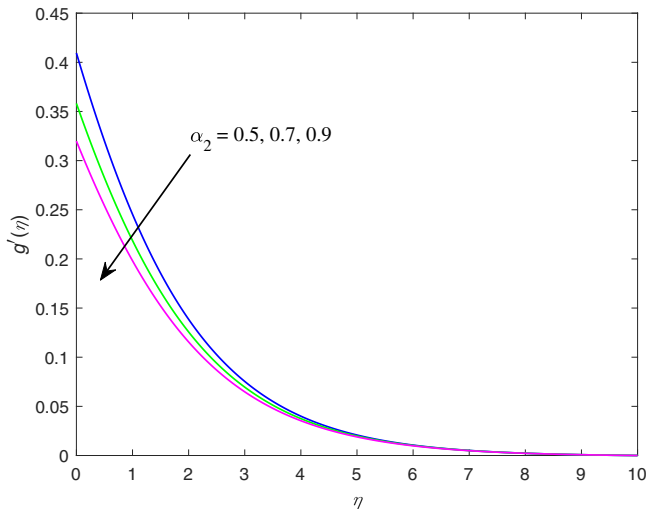


Fig. 7. (Color online)  $g'(\eta)$  under the dominance of  $\alpha_2$ .

is inversely proportional to  $Rd$ . The buoyant force is decreased due to the inefficiency of radiative heat transmission compared to the efficiency of conductive heat transfer. A higher thermal profile is the consequence of high  $Rd$  since it transmits more heat to the working fluids. A greater value of  $Rd$  causes the fluid to become more heated. Because of this, there is a clear increase in heat transfer.

The influence of  $P$  and  $Q$  on fluid temperature is portrayed in Figs. 10 and 11. It is observed that the thermal field produced by the nanofluid flow becomes stronger as

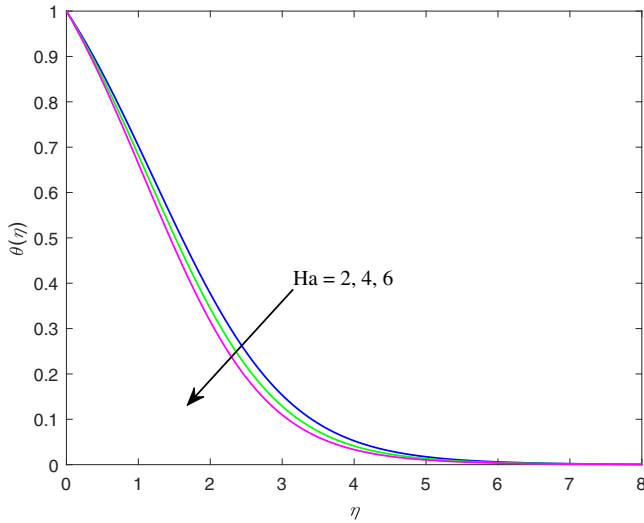


Fig. 8. (Color online)  $\theta(\eta)$  under the dominance of  $Z$ .

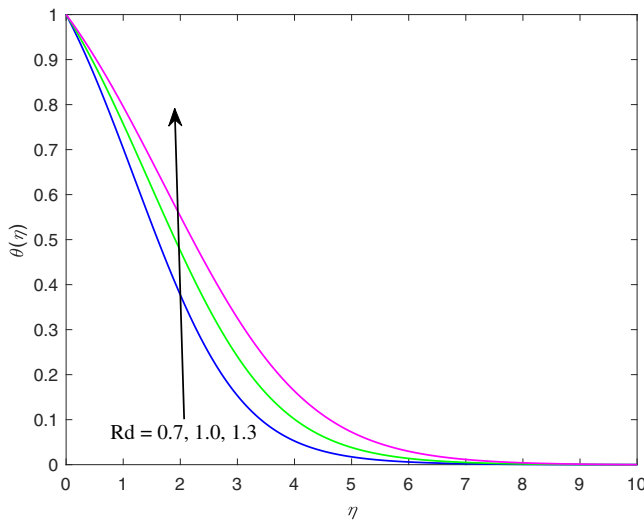


Fig. 9. (Color online)  $\theta(\eta)$  under the dominance of  $Rd$ .

the values of  $P$  and  $Q$  increase. Both  $A$  and  $B$  function as heat generators. The fluid flow temperature goes up when  $P$  and  $Q$  are estimated to be higher. As a result, the thermal field becomes more intense as the values of  $A$  and  $B$  continue to rise. The effect of  $Nb$  on thermal and concentration profiles is illustrated in Figs. 12 and 13, respectively. Figure 12 makes it clear that there is a direct link between  $\theta(\eta)$  and  $Nb$ . For increasing levels of  $Nb$ , there is a corresponding rise in the collision rate between the fluid molecules. So,  $\theta(\eta)$  has been enhanced. Figure 13 shows the change in  $\phi(\eta)$

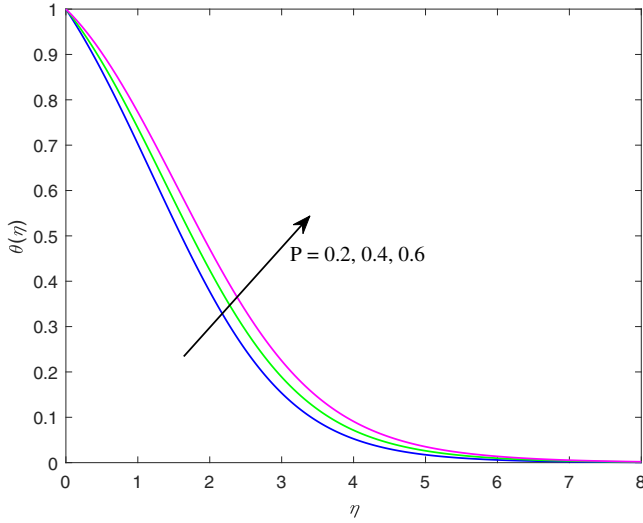


Fig. 10. (Color online)  $\theta(\eta)$  under the dominance of  $P$ .

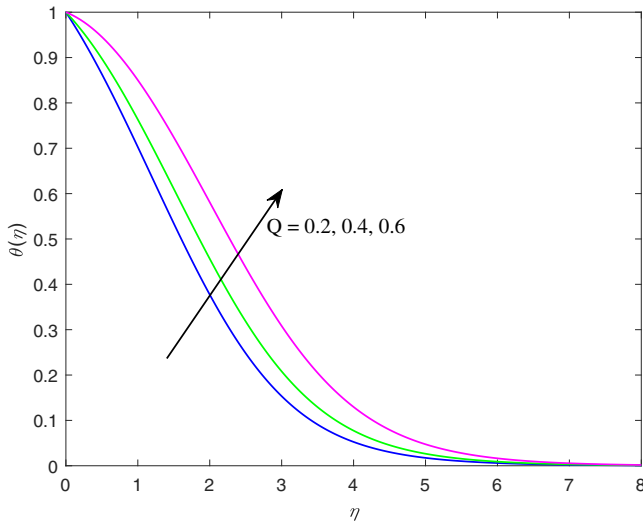


Fig. 11. (Color online)  $\theta(\eta)$  under the dominance of  $Q$ .

as a function of  $Nb$ . The analysis reveals that there has been a decrease in  $\phi(\eta)$  as a result of the increase in  $Nb$ . Physically speaking, when  $Nb$  increases, species concentration falls, and the number of collisions between fluid particles goes up. Figure 14 addresses the properties of  $Nt$  in relation to fluid temperature. There is a proportionate relationship between  $Nt$  and  $\theta(\eta)$ . Thermophoresis is the movement of warm particles from the region of the highest flow temperature to the area of the lowest flow temperature. As a result, a better fluid temperature profile can be

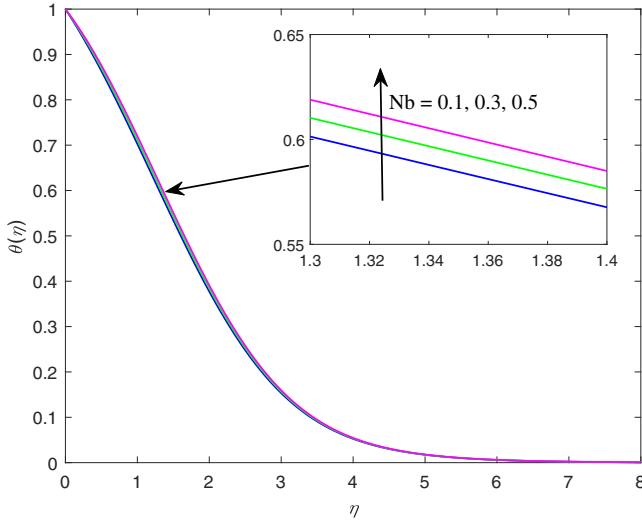


Fig. 12. (Color online)  $\theta(\eta)$  under the dominance of Nb.

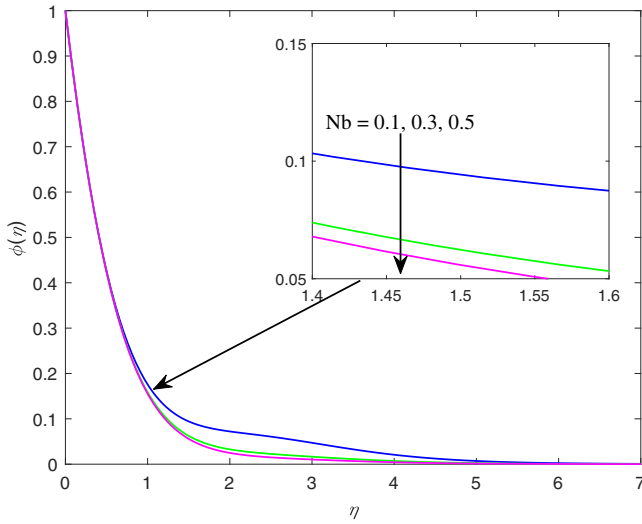


Fig. 13. (Color online)  $\phi(\eta)$  under the dominance of Nb.

achieved with increased values for the thermophoresis parameter. Figure 15 depicts the upshot of Nt on the concentration profile. It is obvious from the graph that there is a direct relationship between Nt and  $\phi(\eta)$ . Particles in a fluid are physically pushed from a hotter surface to a colder one by an enhanced thermophoretic force as Nt rises. So,  $\phi(\eta)$  is stepped up. The variation in concentration field for different  $K_1$  values is noticed in Fig. 16. Insight into the relationship between  $K_1$  and  $\phi(\eta)$  may be gleaned from the graph shown in the figure. The physical reason for this is that as  $K_1$  goes up,

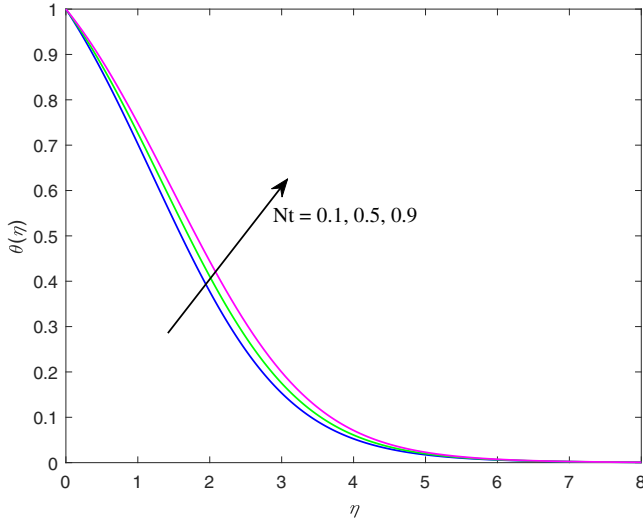


Fig. 14. (Color online)  $\theta(\eta)$  under the dominance of  $Nt$ .

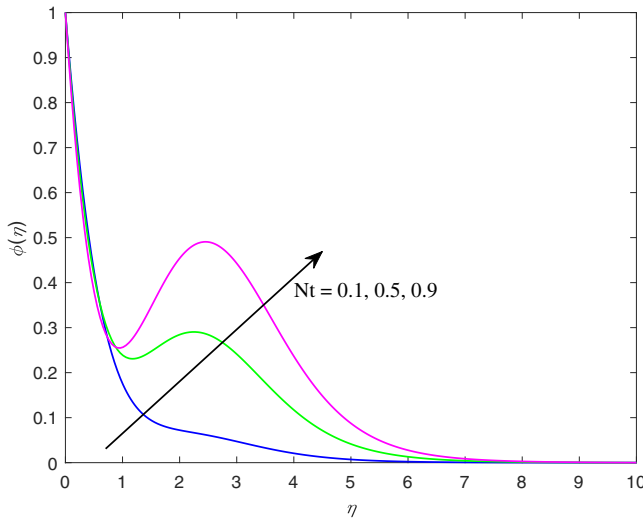


Fig. 15. (Color online)  $\phi(\eta)$  under the dominance of  $Nt$ .

the rate of chemical reactions that cause damage goes up. As a result,  $\phi(\eta)$  goes down. Concentration profile for amplifying values of the activation energy parameter  $E$  is observed in Fig. 17. Here, we see that  $\phi(\eta)$  and  $E$  are directly connected. From a purely physical perspective, higher values of  $E$  emphasize the pace of chemical reaction, which in turn increases  $\phi(\eta)$ .

The coefficients of skin friction, Nusselt number and Sherwood number are determined numerically and presented in Tables 3 and 4. As  $Ha$ ,  $\beta$  and  $\alpha_1$  grow, the

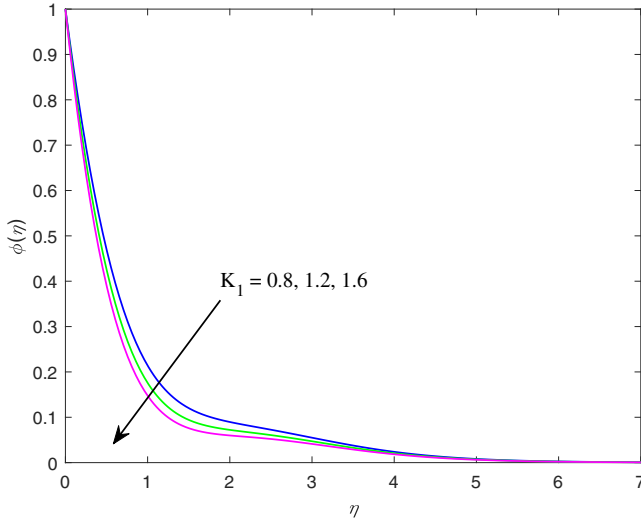


Fig. 16. (Color online)  $\phi(\eta)$  under the dominance of  $K_1$ .

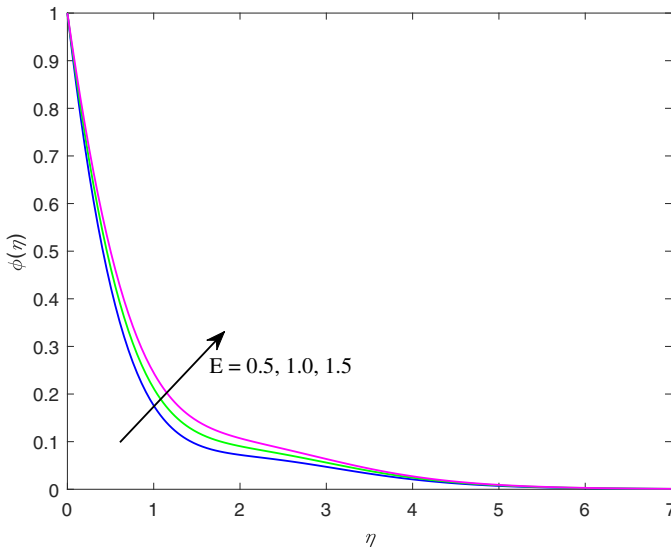


Fig. 17. (Color online)  $\phi(\eta)$  under the dominance of  $E$ .

coefficient of skin friction  $-\sqrt{\text{Re}_x}C_{fx}$  goes down. In contrast,  $-\sqrt{\text{Re}_y}C_{fy}$  rises with increasing  $Ha$  but falls for  $\beta$  and  $\alpha_2$ . Increases in  $Ha$  and  $Rd$  result in a larger Nusselt number  $\frac{Nu_x}{\sqrt{\text{Re}_x}}$ , whereas increases in  $Nb$ ,  $Nt$ ,  $P$  and  $Q$  result in a smaller  $\frac{Nu_x}{\sqrt{\text{Re}_x}}$ . The Sherwood number  $\frac{Sh_x}{\sqrt{\text{Re}_x}}$  significantly rises when  $Nt$  and  $K_1$  are increased, but  $Nb$  and  $E$  strongly suggest the opposite trend.

Table 3. Numerical values of the local skin friction coefficient when  $B = 4$ .

Ha	$\beta$	$\alpha_1$	$\alpha_2$	$-\sqrt{\text{Re}_x} C_{fx}$	$-\sqrt{\text{Re}_y} C_{fy}$
2	0.5	0.5	0.5	0.645323	0.992126
4				0.449852	1.008754
6				0.263408	1.023944
2	1			0.553238	0.896296
	1.5			0.513051	0.854109
	0.5	0.7		0.533080	—
		0.9		0.454887	—
		0.5	0.7	—	0.833797
			0.9	—	0.721130

Table 4. Numerical values of the local Nusselt and Sherwood numbers when  $\text{Pr} = \theta_w = 1.5$ ,  $\text{Le} = 1$  and  $n = 0.5$ .

Ha	Rd	$P$	$Q$	Nb	Nt	$K_1$	$E$	$\frac{\text{Nu}_x}{\sqrt{\text{Re}_x}}$	$\frac{\text{Sh}_x}{\sqrt{\text{Re}_x}}$
2	0.7	0.2	0.2	0.1	0.1	1.2	0.5	0.998989	1.556807
4								1.067195	—
6								1.128348	—
2	1.0							1.095581	—
	1.3							1.163228	—
	0.7	0.4						0.816263	—
		0.6						0.632328	—
		0.2	0.4					0.690805	—
			0.6					0.265353	—
			0.2	0.3				0.927356	1.542879
				0.5				0.860370	1.540355
				0.1	0.5			0.896642	1.702286
					0.9			0.803919	1.893581
					0.1	0.8		—	1.367507
						1.6		—	1.723470
						1.2	1	—	1.390568
							1.5	—	1.257272

### 7. Conclusion

This study investigates the flow of a Casson nanofluid over a Riga plate. The effects of velocity slip, activation energy, and a nonuniform heat source/sink on heat and mass transfer are also considered. It is analyzed how different influencing parameters may affect the flow as well as the heat and mass transport phenomena of the Casson nanofluid. The following are the key findings from this study:

- With increasing velocity slip parameter values, the fluid flow is retarded in both directions.
- Fluid temperature can be enhanced by strengthening the thermal radiation and heat generation processes.
- Increasing the activation energy parameter leads to a higher concentration.

- Raising the modified Hartmann number improves the shear stress at the wall.
- The heat transfer rate may be accelerated by uplifting the thermal radiation and modified Hartmann number.
- Activation energy and chemical reaction are found to reduce the mass transfer rate at the surface.

This study could be expanded to examine effects of entropy generation and radiation absorption on Casson nanofluid flow over a Riga plate.

## Acknowledgments

The first two authors thank National Institute of Technology Meghalaya for providing the necessary facilities to carry out this research. The authors would also want to express their appreciation to the reviewers for their insightful comments and ideas.

## References

1. G. S. Seth, P. K. Mandal and S. Sarkar, *J. Porous Media* **23**, 663 (2020).
2. M. K. Mishra, G. S. Seth and R. Sharma, *Heat Transf.* **49**, 2770 (2020).
3. A. Bhattacharyya *et al.*, *Chin. J. Phys.* **80**, 167 (2022).
4. J. Buongiorno, *J. Heat Transf.* **128**, 240 (2006).
5. M. Mustafa and J. A. Khan, *AIP Adv.* **5**, 77148 (2015).
6. M. J. Babu and N. Sandeep, *Alex. Eng. J.* **55**, 2193 (2016).
7. B. Kumar *et al.*, *Int. J. Therm. Sci.* **146**, 106101 (2019).
8. N. Abbas and W. Shatanawi, *Symmetry* **14**, 1629 (2022).
9. F. Ahmed, R. Mehmood and A. J. Chamkha, *Waves Random Complex Media* (2022), doi: 10.1080/17455030.2022.2125596.
10. S. Ijaz *et al.*, *Waves Random Complex Media* (2022), doi: 10.1080/17455030.2022.2085344.
11. R. Tabassum, R. Mehmood and M. Y. Malik, *Arab. J. Sci. Eng.* **47**, 16319 (2022).
12. E. N. Maraj *et al.*, *Arab. J. Sci. Eng.* **47**, 15875 (2022).
13. G. S. Seth *et al.*, *Proc. Natl. Acad. Sci. India A, Phys. Sci.* **91**, 503 (2021).
14. S. Nandi, M. Das and B. Kumbhakar, *J. Nanofluids* **11**, 17 (2022).
15. B. Kumbhakar and S. Nandi, *Heat Transf.* **51**, 7890 (2022).
16. S. Nandi and S. Nadeem, *Z. Angew. Math. Mech.* **103** (2022) Article ID: e202200380, doi: 10.1002/zamm.202200380.
17. S. M. Hussain *et al.*, *Proc. Inst. Mech. Eng. E, J. Process Mech. Eng.* (2022), doi: 10.1177/09544089221096103.
18. T. A. M. Shatnawi, N. Abbas and W. Shatanawi, *AIMS Math.* **7**, 20545 (2022).
19. P. Nagasantoshi *et al.*, *J. Nanofluids* **7**, 821 (2018).
20. D. V. K. Prasad, G. S. K. Chaitanya and R. S. Raju, *Results Eng.* **3**, 100019 (2019).
21. S. V. Jakati *et al.*, *J. Adv. Res. Fluid Mech. Therm. Sci.* **55**, 218 (2019).
22. G. Kotha *et al.*, *Eur. Phys. J. Plus* **135**, 600 (2020).
23. T. Thumma *et al.*, *Appl. Math. Comput.* **421**, 126927 (2022).
24. K. Mahmud *et al.*, *J. Mol. Liq.* **352**, 118732 (2022).
25. S. Nandi and B. Kumbhakar, *Phys. Scr.* **96**, 125225 (2021).
26. S. Nandi and B. Kumbhakar, *Indian J. Phys.* **96**, 2873 (2022).
27. M. Das, S. Nandi and B. Kumbhakar, *Palest. J. Math.* **11**, 95 (2022).
28. M. Das, B. Kumbhakar and J. Singh, *J. Comput. Anal. Appl.* **30**, 176 (2022).

29. M. Das and B. Kumbhakar, *Proc. Inst. Mech. Eng. E, J. Process Mech. Eng.* (2022), doi: 10.1177/09544089221147386.
30. T. Hayat *et al.*, *Phys. A, Stat. Mech. Appl.* **549**, 124006 (2020).
31. A. Dawar, Z. Shah and S. Islam, *Heat Transf.* **50**, 2558 (2021).
32. A. Shahid *et al.*, *J. Therm. Anal. Calorim.* **143**, 2585 (2021).
33. M. Das and B. Kumbhakar, *J. Porous Media* **25**, 17 (2022).
34. Z. Iqbal *et al.*, *Commun. Theor. Phys.* **69**, 68 (2018).
35. P. Loganathan and K. Deepa, *J. Theor. Appl. Mech.* **57**, 987 (2019).
36. H. Vaidya *et al.*, *Case Stud. Therm. Eng.* **24**, 100828 (2021).
37. A. M. Obalalu *et al.*, *Eur. Phys. J. Plus* **136**, 891 (2021).
38. S. M. Hussain, R. Sharma and S. S. Alrashidy, *AIP Conf. Proc.* **2435**, 20002 (2022).
39. N. Abbas and W. Shatanawi, *Energies* **15**, 4945 (2022).
40. T. A. M. Shatnawi, N. Abbas and W. Shatanawi, *Mathematics* **10**, 3573 (2022).
41. N. Abbas *et al.*, *Waves Random Complex Media* (2022), doi: 10.1080/17455030.2022.2111029.
42. K. Mahmud *et al.*, *Int. J. Heat Mass Transf.* **138**, 106347 (2022).
43. R. Tabassum *et al.*, *Int. Commun. Heat Mass Transf.* **135**, 106165 (2022).
44. T. Abbas, M. M. Bhatti and M. Ayub, *Proc. Inst. Mech. Eng. E, J. Process Mech. Eng.* **232**, 519 (2017).
45. A. K. A. Hakeem *et al.*, *J. Appl. Comput. Mech.* **6**, 1012 (2020).
46. E. O. Fatunmbi and A. Adeniyani, *Results Eng.* **6**, 100142 (2020).
47. A. M. Obalalu *et al.*, *Heat Transf.* **51**, 3951 (2022).
48. C. Y. Wang, *Phys. Fluids* **27**, 1915 (1984).
49. K. G. Kumar *et al.*, *Results Phys.* **7**, 3465 (2017).
50. P. Ragupathi *et al.*, *J. Heat Mass Transf. Res.* **8**, 49 (2021).